Archives of Civil and Mechanical Engineering (2021) 21:148
https://doi.org/10.1007/s43452-021-00297-1

ORIGINAL ARTICLE

The influence of plasma-sprayed coatings on surface properties and corrosion resistance of 316L stainless steel for possible implant application

Anna Woźniak[1] · Marcin Staszuk[1] · Łukasz Reimann[2] · Oktawian Bialas[1] · Zbigniew Brytan[1] · Sergii Voinarovych[3] · Oleksandr Kyslytsia[3] · Sergii Kaliuzhnyi[3] · Marcin Basiaga[4] · Marcin Admiak[2]

Received: 15 March 2021 / Revised: 2 August 2021 / Accepted: 19 August 2021 / Published online: 12 September 2021

Abstract
Herein, we analyzed the morphology of atmospheric plasma-sprayed (APS) coating on medical 316L stainless steel and its influence on the physical and electrochemical properties of implant application. Five types of coatings were examined: hydroxyapatite (HAp), titanium (Ti), zirconium (Zr), Ti/HAp and Zr/HAp. The base properties of the coatings were analyzed via chemical and phase composition, surface topography, surface wettability and in particular the corrosion resistance in Ringer solution in immersed conditions and potentiodynamic test, and EIS analysis. APS coating of pure HAp on 316L stainless steel showed poor cohesive bonding to the substrate material, whereas the application of Ti and Zr interlayer prior to HAp deposition improved surface morphology and coating properties. The beneficial effect of Ti and Zr interlayer under HAp layer on binding was demonstrated. HAp containing coatings (HAp, Ti/HAp and Zr/HAp) show Ca/P ratio greater than 1.8, which may positively influence the differentiation of osteogenic cells and good adhesion to bones. Among the studied materials, the composite coatings with Zr or Zr/HAp showed favorable physicochemical properties and the highest corrosion resistance in Ringer solution.

Keywords 316L stainless steel · Plasma spray coating · Hydroxyapatite (HAp) coatings · Corrosion · EIS · Contact angle

1 Introduction

In 1977, Brånemark [1] defined the osseointegration phenomena as a sequence of processes starting immediately after fixing the implant into a previously prepared cavity. Due to the bone cavity reaming, an implant can be surrounded by blood, as well as both dead and living bone tissue. Hence, the implanted material is exposed to a biochemically dynamic environment that tends to react causing corrosion/ionization. In addition to material weakening during the corrosion process, there is a risk of the tissue reacting, promoting the release of corrosion products from the implant inside the body [2]. Ions deposited in the surrounding tissues lead to metallosis and cytotoxic effect in the implant cavity generating necrosis and complete implant failure [3]. The fundamental requirement of a biomaterial is that both material and the tissue environment of the body should coexist without any undesirable or inappropriate effects toward each other. Therefore, avoidance of corrosion is necessary when the implant resides inside the cavities of a human body [2].

Basic corrosion types commonly observed in the human body include selective dissolution, pitting, fretting corrosion, intergranular corrosion, etching and crevice corrosion, to name a few. The most common corrosive processes involve the formation of local corrosion cells. Such material degradation occurs when two different metals in terms of

✉ Anna Woźniak
anna.wozniak@polsl.pl

[1] Department of Materials Engineering and Biomaterials, Faculty of Mechanical Engineering, Silesian University of Technology, Konarskiego 18A Street, 44-100 Gliwice, Poland

[2] Materials Research Laboratory, Silesian University of Technology, Konarskiego 18A Street, 44-100 Gliwice, Poland

[3] E.O. Paton Electric Welding Institute of the National Academy of Sciences of Ukraine, 11 Kazymyr Malevych St., Kyiv 03150, Ukraine

[4] Faculty of Biomedical Engineering, Silesian University of Technology, Roosevelta 40, 41-800 Zabrze, Poland

microstructures and compositions interact with the environment filled with electrolytes. In the case of the human body, electrolytes are vital fluids that have contact with the implanted material [4]. During corrosive decomposition of the material, ions are released into nearby tissues causing an immune system response, which results in inflammation, including temperature increase of soft tissues in the immediate vicinity of the implant. According to van't Hoff's rule, the speed of the chemical reaction increases by two to four times when the temperature increases by 10 °C, which also accelerates the corrosion processes in the tissue–implant system, leading to acceleration of the entire process in the loop [5].

Other than Ti, 316L stainless steel has been the lead material in dentures and orthopedic replacements for the last decades [6]. The utility of austenitic stainless steel 316L type is related to efficient biocompatibility, corrosion resistivity and cost [7]. Nevertheless, 316L family cannot support long-lasting bone tissue survivor, which leads to osteosclerosis, lowering bone–implant–connection ratio (BIC) and implant failure [8]. Prolongation of the implant's life cycle inside the body has been extensively studied [9]. The majority of reports are based on surface expansion to fix the implant properly and then to increase corrosion resistance [10], i.e., grinding, etching, laser surface texturing [11], plasma spraying, etc., [12] combined with various coatings, i.e., Ti, TiN, TiO_2 [13], Zr, ZrO_2 [14], hydroxyapatite (HAp) [15], and Al_2O_3 [16]. Hybrid treatment of implant materials is aimed at providing adequate influence of the surrounding tissues, and among many properties, the most important is significantly enhanced corrosion resistance [17].

Stainless steel, Ti and Co alloy implants are widely plasma spray coated with HAp to inhibit the corrosion rate, where HAp ceramic coating degrades incomparably slowly and promotes the early formation of strong bonds between the metal implant and living bone [18]. The plasma spray coating process involves heating the HAp powder to a semi-molten or molten state and deposition through the plasma flame on the substrate material. Although the plasma temperature is high (6000–16,000 °C), the substrate surface temperature remains below 150 °C [19]. One major advantage of HAp coating is its ability to further dope with ions and substitute part of its structure with metallic agents (i.e., Zn, Cu, Ag, Fe, Ti, Mg, Ni, Cr, Mn, Co, Sr, Pb, Cd and many others) implemented because of their antibacterial property and lack of cytotoxicity at low concentrations. Ding et al. [19] reported that Zn-substituted HAp (Zn-HAp) coatings fabricated on pure Ti revealed improved biocompatibility and corrosion resistance. Incorporation of Zn^{2+} into HAp structure significantly reduced porosity and caused the coating to become noticeably denser. Furthermore, HAp coatings enriched with Ti (Ti/HAp) display significant improvement of in vitro corrosion performance of metallic implant substrates [20]. Previous research has found that TiO_2/HAp has better stability than HAp monolayers [5]. Nevertheless, it has been described that the use of Ti as an alloying element with other corrosion-resistant elements enhances the stability of Ti layer, which further increases corrosion resistance [21]. Ti itself is known as the most common metallic biomaterial for long-lasting implantation in dental and orthopedic application. Among other materials, Ti is distinguished by its ability to form a spontaneous passive layer of TiO_2. However, this layer does not provide satisfactory corrosion protection due to defects such as inclusions, discontinuity and weak spots, which can become the initial areas of corrosion [10]. Zirconium–HAp (Zr/HAp) is non-toxic and allergy-free substance presenting high resistance to corrosion and with perspective to be used for medical implants. Zr and Ti belong to the same group in the periodic table; hence, they are expected to present increased corrosion resistance properties of base material and should be taken into account in the following comparative research [22]. Nevertheless, the physical and chemical properties of Ti and Zr, as well as their oxides, such as oxidation rates, crystal structures, transport properties and water interactions, differ quantitatively. Furthermore, the E-modulus of Zr is 88 GPa (Ti about 110 GPa), which is similar to that of bone [23]. Ultimately, Ti does not require a stabilizer, whereas Zr in its most mechanically favorable cubic form is stabilized with Y_2O_3 [24]. As Y_2O_3 concentration increases, the temperature of Zr cubic form decreases [25].

Herein, HAp coating application constituted by the plasma-spraying approach was examined. Hydroxyapatite HAp is a calcium phosphate mineral $Ca_{10}(PO_4)_6(OH)_2$ of the apatite group and is a chemically similar compound to that of natural bone. HAp powder thermal sprayed on the implant's surface is not achievable for metals in corrosion rate and has a great affinity to the host bone. Thus , increased bone-to-implant contact ratio (BIC ratio) can be achieved [26]. It has been previously proposed that to improve the bioproperties of the implant and rapid accretion with the bone, the implant surface should be coated with a highly corrosive-resistant coating with a large surface morphology [27]. Suggested pore sizes of the coating range from 20 to 200 μm and closed porosity is at least 30% [28]. Augmentation of the surface area prevents hindrance of corrosion resistance due to the reactivity, which increases proportionally with the reactant surface area's growth [29]. The following research combines Hap with Zr and Ti ions allowing atmospheric plasma-sprayed APS coatings on 316L stainless steel. Determination of the corrosion resistance and benefits of the surface morphology during the deposition process's various conditions was possible. Based on structural characterization, the plasma spraying deposition process parameters were selected. The coatings were studied by XRD, SEM, and EDS analysis. The corrosion EIS tests were also

Table 1 Chemical composition of 316L stainless steel

Element, wt. [%]	Cr	Ni	Mo	C	Si	Mn	Nb	P	S	N	Cu	Fe
Declared	19.00–21.00	10.00–11.00	2.00–3.00	≤0.03	≤1.00	≤12.00	0.25–0.80	≤0.04	≤0.03	≤0.10	≤0.25	Rest
ISO 5832-9	19.50–22.00	9.00–11.00	2.00–3.00	0.08	0.75	2.00–4.25		≤0.02	≤0.01	0.25–0.50	–	Rest
Measured	19.50	10.60	2.50	–	0.70	3.00	–	≤0.02	≤0.01	–	–	Rest

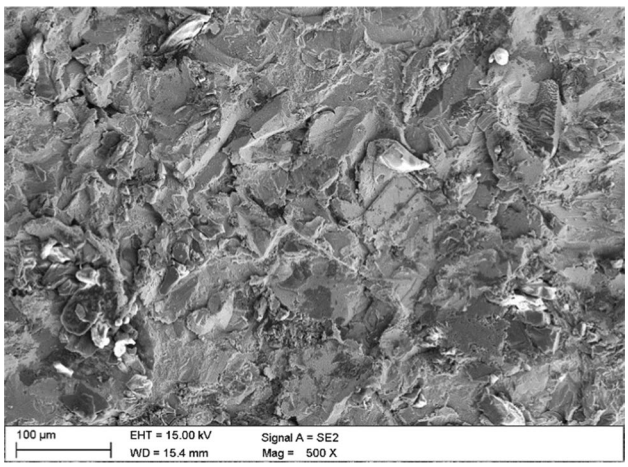

Fig. 1 Surface morphology of sandblasted sample

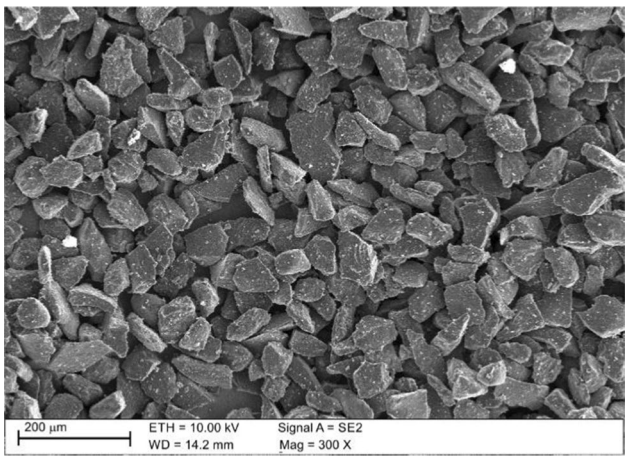

Fig. 2 SEM image of hydroxyapatite raw powder

examined. The surface chemistry characterization in view of the bioproperties was determined, as well as the wetting angle and free surface energy.

2 Materials and methods

Austenitic stainless steel 316L (medical), the substrate material, was subjected to plasma spray coating . Table 1 shows the chemical composition of stainless steel used, which meets the requirement ISO 5832-9 standard (implants for surgery: metallic materials, wrought high nitrogen stainless steel) [30].

Prior to conducting the plasma spray coating process, 316L samples were subjected to mechanical grinding via grinding with MD-Piano abrasive cloth —MD- Piano 200, 600 and 1200 (Struers, Ballerup, Denmark). Finally, all samples were cleaned sequentially in acetone and deionized water with ethanol (2:1), using ultrasonic cleaner InterSonic IS-1 (InterSonic S.C., Olsztyn, Poland) and then dried. Then samples were subjected to sandblasting to obtain good adhesive bonding between substrate material and coating (Fig. 1). The average surface roughness of 316L samples was in the range of 1.2 ± 0.3 µm.

Subsequent samples were subjected to surface modification by atmospheric plasma spraying (APS) using the MPS-004 Microplasma spraying system (E.O.Paton Electric Welding Institute, Ukraine, Kyiv), equipped with a power source and control panel, plasmatron, special powder and wire feeders. The coatings were deposited by spraying molten metal [zirconium (Zr) and titanium (Ti)] provided as a 0.3 mm diameter wire. Additionally, HAp BioMin (NPO RAPID, Ukraine, Kyiv) high-purity (> 99%) powder with particle size of 40–65 µm was used for the APS process (Fig. 2). The powder was originally designed and produced to deposit coatings on metal implants. It mainly had a fragmented shape; however, due to the rolling operation, the corners of many particles were smooth, which ensured its good fluidity (68–75 s/50 g). Additionally, the powder particle was irregular in shape. The powder was a compact agglomerate.

The powders (HAp and doping elements Ti and Zr) melted by the plasma arc were deposited on 316L stainless steel substrate. To investigate the synergistic effect of the mentioned powders, gradient coatings were applied. The functional gradient coating was deposited in two layers: (1) underlayer of Zr or Ti and (2) top layer of sprayed HAp coating (Table 2).

Table 3 summarizes the APS process parameters. Argon (Ar) was used as the carrier gas to form the plasma. After APS process and any loose embedded powder particles were removed, all samples were exposed to the compressed air.

High-resolution scanning electron microscope SEM Supra 35 (Zeiss, Oberkochen, Germany) was used to

Table 2 List of studied coating types on 316L stainless steel

No	Name	Coating material	Base material
1	316L_HAp	HAp	316L
2	316L_Zr	Zr	
3	316L_Ti	Ti	
4	316L_Zr/HAp	Zr/HAp	
5	316L_Ti/HAp	Ti/HAp	

characterize the surface morphology. The observations were carried out at a magnification of 100 $x-20$ kx and accelerating voltage ranging from 10 to 15 kV. Additionally, the coating cross section was studied to determine the thickness of the deposited coating material and characterize the morphology of deposited composite coating material. Firstly, the samples were cut using a metallurgical saw by precision-cut saw Secotom-50 (Struers, Ballerup, Denmark), then mounted in epoxy resin using an automatic press for hot mounting CiroPress-30 (Struers, Ballerup, Denmark). Next, the cross-sectioned samples were ground according to the previously described procedure and polished using colloidal suspension OPU-4 to achieve a mirror-finished surface. Elemental analysis was performed by energy-dispersive X-ray spectrometry with an EDS detector (Mahwah, NJ, USA) during SEM analysis. Before microscopic observation, the surface was sputtered with a thin conductive gold–palladium film using sputter coater SCD050 (BAL-TEC, Los Angeles, USA). Surface topography examination was conducted using digital 3D microscope DVM6 (Leica Microsystems, Wetzlar, Germany).

The phase composition was characterized by X-ray diffraction using X'Pert PRO X-ray diffractometer (Panalytical, Almelo, Netherlands). The phase identification was performed using Cu Kα radiation with 2θ ranging from 20° to 90° with a step of 0.05°. The voltage of Cu lamp and current of heater were set to 40 kV and 30 mA, respectively.

Adhesion of the tested coatings to the base material 316L stainless steel was performed by a scratch test method using open platform CSM. The test was conducted by generating a scratch using a Rockwell diamond cone with a gradual increase of the penetrator loading force. To estimate the critical force L_c (the minimum normal force that causes loss of the adhesion of coating to the substrate material), the results of acoustic emission signal changes, friction force as well as optical microscope observations were used. The tests were carried out with loading force increasing in the range of $F_c = 0.03–30$ N. The following operating parameters were applied: scratch length $l = 3$ mm; loading rate $V_s = 10$ N/min, and table speed $V_t = 1$ mm/min.

The physicochemical properties of the studied coatings were determined by contact angle θ measurements using the sitting drop method and surface free energy (SFE) calculation via Owens–Wendt method. The measurements were performed using Surftens Universal goniometer (OEG, Frankfurt, Germany) and PC with Surftens 4.5 software to analyze recorded drop images. The distilled water θ_w (POCH S.A., Gliwice, Poland) and diiodomethane θ_d (Merck, Warsaw, Poland) were used as a measure liquid, and droplets of each 1.5 μm^3 volume were placed on the tested surface. The measurements were carried out at room temperature $T = 23 \pm 1$ °C (289 K) over $t = 60$ s with a sampling rate of 1 Hz. Based on the determined water and diiodomethane contact angle, the values of SFE and their polar and apolar components were calculated (Table 4).

The corrosion resistance of the coatings was examined using the potentiodynamic method by recording anodic polarization curves, according to PN ISO 17475:2010 standard [32]. The test stand comprised Atlas 0531 EU potentiostat (ATALS-SOLLICH, Rębiechowo Poland) and a typical three-electrode system, which included a Pt wire (auxiliary electrode), silver/silver chloride electrode (Ag/AgCl) (reference electrode) and the tested sample (working/anode electrode). First, the open circuit potential E_{OCP}

Table 4 The values of surface free energy (SFE) and their components for distilled water and diiodomethane obtained using Owens–Wendt method [10, 31]

Liquid	SFE [mJ/m^2]		
	γ_L	γ_L^d	γ_L^p
Distilled water	72.80	21.80	51.00
Diiodonomethane	50.80	50.80	0

Table 3 Parameters of the atmospheric plasma-spraying (APS) process

Coatings	Parameters						
	Plasma current I [A]	Plasma voltage [V]	Flow rate V_w [g/min]	Primary gas flow Ar [SLPM]	Shilding gas flow Ar [SLPM]	Nozzle diameter [mm]	Standoff distance (SOD) [mm]
HAp	40	30	1.2	80	400	1	60
Zr	18	37	2.2	180	600	1	70
Ti	19	37	1.5	180	600	1	80

was monitored for $t = 1$ h. The corrosion tests started from the initial potential to the fulfillment of one of the conditions of the experiment: when the potential reached 2 V or through the current density of 1 mA /cm^2 curves ranging from − 1 to + 1 V at a scanning rate of 1 mV/s. Based on the recorded curves, the parameters characterizing the corrosion resistance were determined: corrosion resistance (E_{corr}), transpassivation potential (E_{tr}) or breakdown potential (E_b), repassivation potential (E_{cp}), the value of polarization resistance (R_p), corrosion current density (i_{corr}), and the Tafel component of the anodic slope (b_a) and cathodic slope (b_c). To evaluate the influence of the coating porosities on the corrosion resistance and Tafel slope, the porosity of the coatings was calculated by Elsener's equation Eq. (1), where P—porosity; $R_{p,substrate}$—the substrate polarization resistance; $R_{p,coating}$—the coating polarization resistance; $\Delta E_i = 0$—the difference between the corrosion potentials of the coatings and substrate; and b_a—the substrate anodic slope:

$$P = \left(\frac{R_{p,substrate}}{R_{p,coating}}\right) \cdot 10^{\frac{|\Delta E_i = 0|}{b_a}}. \quad (1)$$

Additionally, to evaluate the protective efficiency P_e of the surface layer/coating, Eq. (2) proposed by Nozawa and Aramaki [33] was used, where $i_{corr,substrate/coating}$—the substrate/coating current density [34, 35]:

$$P_e = \left(1 - \frac{i_{corr,coating}}{i_{corr,substrate}}\right) \cdot 100\%. \quad (2)$$

A more detailed understanding of the corrosion behavior of the studied coatings and determination of the characteristics and quality of the produced layers was obtained by electrochemical impedance spectroscopy (EIS) analysis using the identical test stand to that of the corrosion resistance test. EIS frequency ranged from 10^4 to 10^{-3} Hz, and the voltage amplitude of the sinusoidal signal was 10 mV. Testing revealed the impedance spectra of the circuit, which was presented in the form of Nyquist plot (a real-imaginary impedance curve) and Bode diagram (curves representing the frequency dependence on the impedance and phase shift). The recorded impedance spectra were adjusted to the equivalent electrical circuits, using the least-squares method. Based on this approach, the values of resistance R and capacity C were determined.

Data reproducibility was examined by conducting three tests on two different samples prepared under the same conditions for each sample group. To simulate the conditions prevailing in the human body, the potentiodynamic and electrochemical tests in Ringer solution of neutral pH = 7.4 at human body temperature $T = 37$ °C were performed (NaCl—8.6 g/cm^3, KCl—0.3 g/cm^3, $CaCl_2 \times 2H_2O$—0.33 g/cm^3).

3 Results

Figure 3 shows the surface morphology of all coated samples analyzed by SEM. SEM analysis shows heterogeneous and rough surface characteristics of the samples with HAp coatings in the presence of partially melted spherical particles and melted regions with smooth glassy regions, i.e., amorphous areas (Fig. 3a). According to the cross-sectional micrographs, the thickness of HAp coating is in the range of 125 ± 37 µm (Fig. 3b). Additionally, a high amount of pores are observed, which are unevenly distributed throughout the entire volume of the HAp coating. The coating and substrate material interface indicates that HAp has very poor cohesive bonding to the 316L substrate material, which is caused by the high brittle nature of HAp that has been also noted by Singh et al. [13]. Samples with Ti and Zr coatings show typical plasma-sprayed features (from the metallic wire) such as solidified splats of fully or partially melted individual particles (Fig. 3c, e) over the surface and clear lamellar structure (Fig. 2d, f) [16, 36]. The splats consist of high ridges of splattered deposited molten metal and melted regions, which are related to the discharge channels (Fig. 2c–f). Unmelted or partially melted spherical particles can also be observed near the surface of the spots [16]. Particle size is in the range of 1–12 µm, and the results are comparable to those reported by Kumari et al. [37]. As shown in Fig. 3d, f, the splats obtained on the surface of Ti and Zr coatings have a similar area. Further observation of Ti and Zr coatings show the presence of periodic macrocracks perpendicular and parallel to the coating/substrate interface. Cracks oriented perpendicular are generally defined as segmentation cracks, which channel across the coating forming a crack network (mud cracks) [38]. According to the cross-sectional micrographs shown in Fig. 3d, f, h, j, the vertical cracks do not pierce through the single coating layer, but are limited within one single flattened particle. Similar results for ceramic-sprayed coatings have been reported by Mifune et al. [39]. The melted Ti and Zr particles collide on the substrate material or existing previously layer spread and are rapidly cooled. In effect, the particles of Ti or Zr coating material strongly adhere to one another or 316L substrate material, guaranteeing a stable, cohesive bond (Fig. 3d, f). The thickness of Ti and Zr coating are approximately 211 ± 25 µm and 320 ± 29 µm, respectively. However, Ti coating shows more defects compared to Zr coating. The top surface morphology of composite coatings Ti/HAp and Zr/HAp is less defective than that of a single HAp layer. Furthermore, the surface is comparatively denser than Hap-coated surface. Additionally, for samples with composite coating Ti/HAp or Zr, the positive effect on the adhesion of HAp with the substrate is

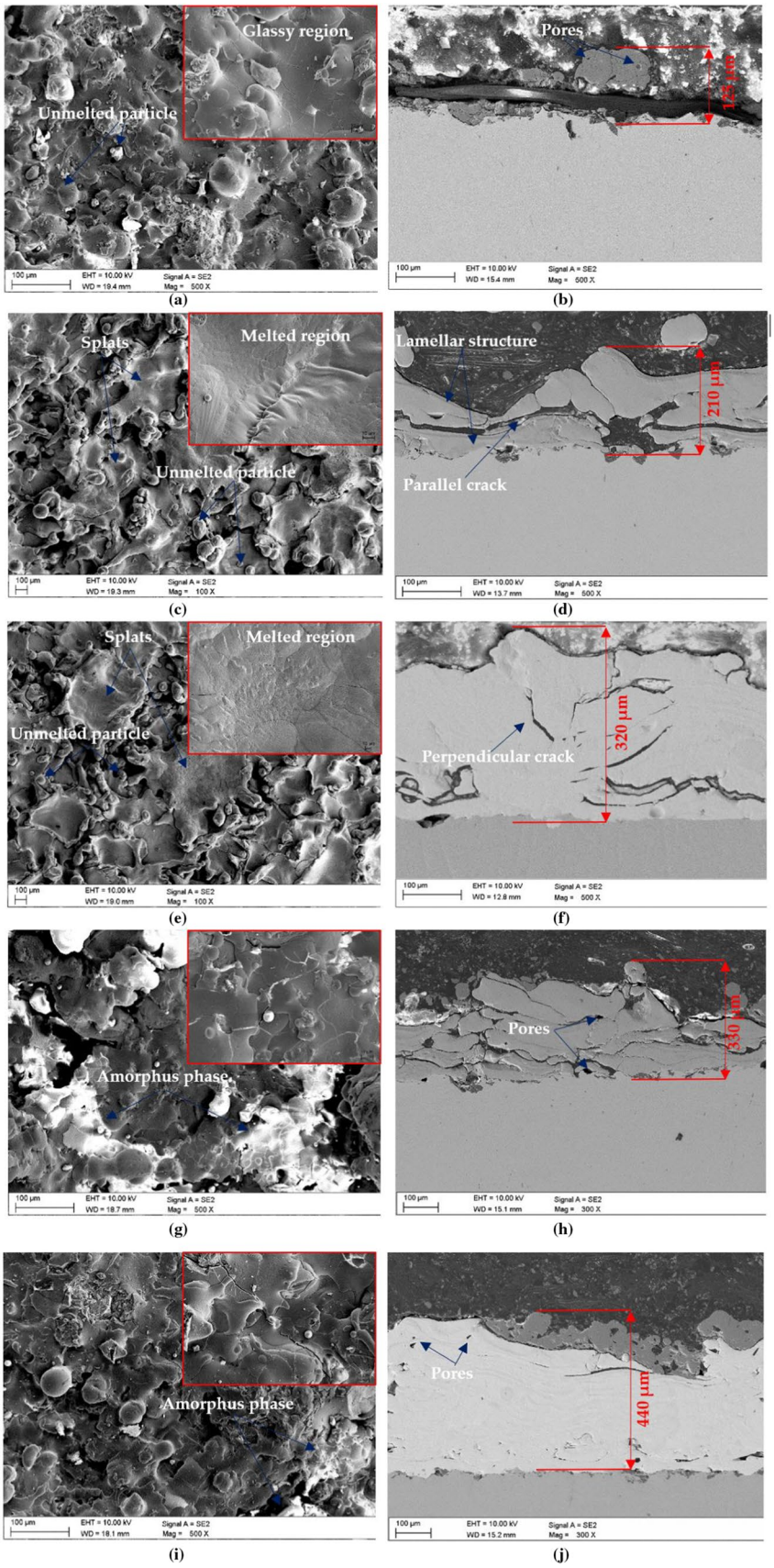

Fig. 3 Example of surface morphology, SEM observation of studied coatings: **a**, **b** HAp coating; **c**, **d** Ti coating; **e**, **f** Zr coating; **g**, **h** Ti/HAp coating; **i**, **j** Zr/HAp coatings

observed (Fig. 3l, h, j). HAp particles fully mapped the morphology of Ti and Zr coatings. Significantly fewer HAp discontinuities are observed for Ti or Zr/HAp samples than HAp coating. The thickness of the composite layers is a combination of the thickness of its components, and the mean values are 350 ± 37 µm and 410 ± 43 µm, respectively, for Ti/HAp and Zr/HAp coatings.

The chemical formula of stoichiometric HAp is $Ca_{10}(PO_4)_6(OH)_2$, where the calcium to phosphor (Ca/P) ratio significantly affects the biointegration and human body environmental response after the implantation process. Generally, standard Ca/P ratio for HAp is 1.67 [40, 41]. However, when Ca/P ratio ranges from critical value 1.67–2.0, strong adhesion of HAp to the bone can be observed. EDS analysis shows the presence of Ca, P, and O elements along with base elements and confirmed the growth of apatite (Fig. 4). EDS microchemical analysis of HAp coatings confirm that for all types, Ca/P ratio values vary from 1.8 to 1.9, which are relatively close to the value range for stoichiometric Hap, thus good adhesion to the bone is expected.

Figure 5 shows XRD diffractograms of base material 316L stainless steel and the studied coatings. The identified diffraction planes of 316L stainless steel indicate a fully austenitic microstructure. Other diffraction peaks from the titanium α (Ti_α) were recorded (ICSD code 98-004-3416). Additionally, for Zr coating, XRD analysis identified the presence of diffraction peaks from two crystallographic zircon varieties—cubic (ICSD code 98-004-1511) and hexagonal (ICSD code 98-004-9700). For other samples, only diffraction peaks from the coating's materials were identified. The XRD pattern of Hap-coated samples mainly shows the crystalline phases (ICSD no. 96-101-1243). The XRD peak is observed at diffraction angle 30.5°, owing to the disintegration of HAp as a consequence of thermal sequence and speedy cooling during the APS process. In the case of composite coatings, XRD analysis identified only the fractional patterns derived from the crystalline structure of HAp. Therefore, HAp forms a dense layer on the surface of Ti and Zr coatings.

The surface topography evaluated by 3D microscope (Fig. 6) is consistent with SEM surface morphology results. The uncoated stainless steel (316L) surface is characterized by a relatively uniform surface roughness resulting from the grinding and sandblasting process, and the mean value of surface roughness, measured by a profilometer, is $R_a = 3.50 \pm 0.40$ µm. Deposition of HAp coating slightly increases surface roughness, and the mean value of 316L_HAp samples is $R_a = 5.20 \pm 1.2$ µm. The surface topography indicates that samples with HAp coating are rough and porous, and HAp powder evenly covers the coating's surface. In the case of Ti and Zr coatings, the surface topography reveals splats with a mean height of approximately 0.35 ± 0.08 µm. Hills and valleys (micro

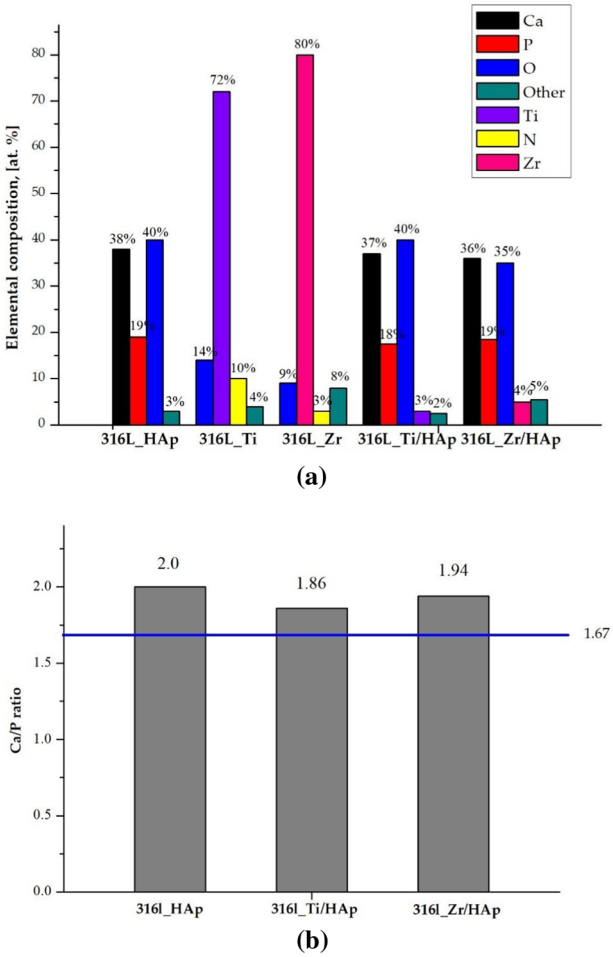

Fig. 4 Examples of microchemical analysis; **a** elemental composition of coated samples; **b** Ca/P ratio for samples with HAp, Ti/HAp and Zr/HAp coatings

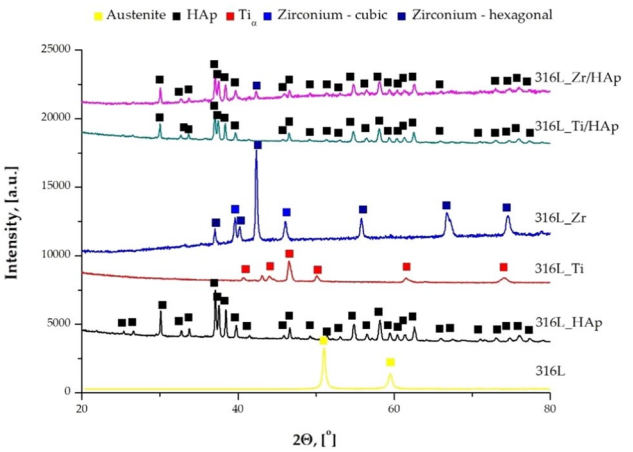

Fig. 5 XRD patterns of base material (316L) and studied coatings: Zr/HAp, Ti/HAp, Zr, Ti and HAp

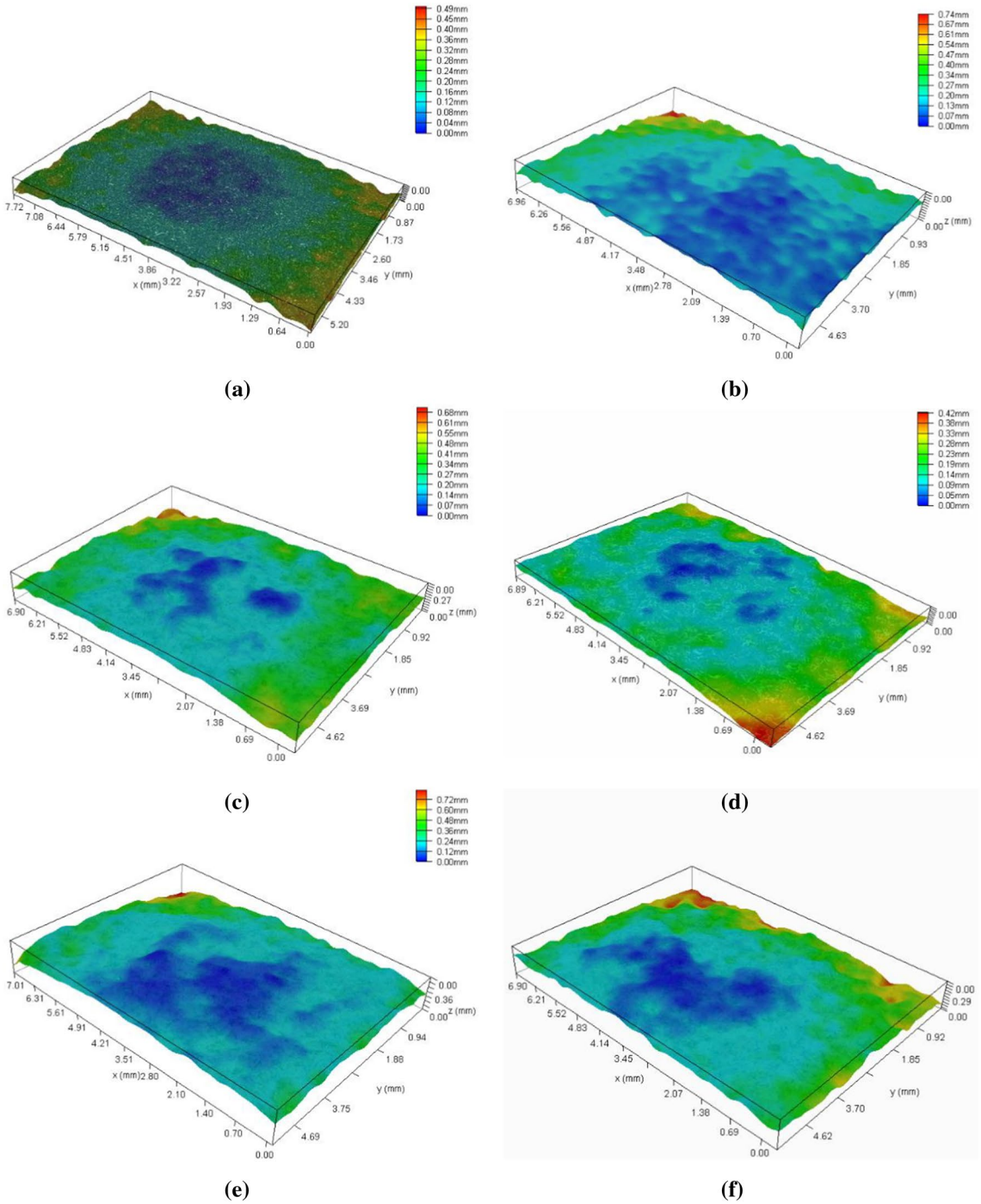

Fig. 6 Surface topography of **a** sandblasted substrate 316L and coatings: **b** HAp coating; **c** Zr coating; **d** Ti coating; **e** Ti/HAp coating; **f** Zr/HAp coating

discharge regions) on Ti and Zr surfaces can be observed over a large area 7 mm × 5 mm. However, Zr coating shows a greater frequency of splats in the area observed. In effect, the presence of periodical splats and surface roughness of these coatings is higher than in the HAp coating, and the surface roughness is more than $R_a = 15 \pm 1.2$ µm and $R_a = 16 \pm 1.0$ µm, respectively, for Ti and Zr coatings. Deposition of HAp powder on Ti/HAp or Zr/HAp coatings leads to partial filling of the spaces between splats. However, mapping of the surface roughness is mainly observed for the coatings. In the case of composite coatings (Ti and

Table 5 Results of scratch test of HAp, Ti and Zr coatings to the substrate material

No.	Coating	Failure of the layer	The value of registered indenter load Fn [N]
1.	316L_HAp	Spallation L_{c2}	6.6
		Complete break L_{c3}	13.5
2.	316L_Ti	Spallation L_{c2}	7.4
		Complete break L_{c3}	> 30
3.	316L_Zr	Spallation L_{c2}	14.8
		Complete break L_{c3}	> 30
4.	316_Ti/HAp	Spallation L_{c2}	8.40
		Complete break L_{c3}	> 30
5.	316_Zr/HAp	Spallation L_{c2}	14.8
		Complete break L_{c3}	> 30

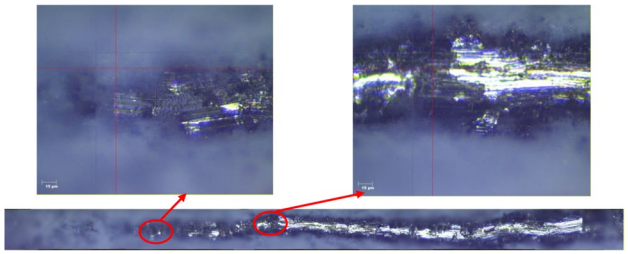

Fig. 7 Example of scratching on 316L_HAp samples

Zr /HAp), slight changes in roughness may be observed, with a value of $R_a = 13 \pm 1.2$ µm.

To evaluate the adhesion of coatings to the base material 316L stainless steel, two main failures were investigated—spallation (L_{c2}) and complete break (L_{c3}). Table 5 presents L_c values that are attributed to the specific failure modes for HAp, Ti and Zr coatings. Both L_c values of the adhesion layer (Ti and Zr) are significantly higher than those of the HAp coatings. The best substrate adhesion is found in Zr coating applied on the substrate material. However, the mechanical nature of scratches for all samples is similar. An example of scratching on the 316L_HAp samples is shown in Fig. 7. In the first step of the test, spallation as a type of scratch failure of the layer is observed. For the HAp and Ti coating, spallation is observed in intervals of 6.6 (HAp) to 7.4 N (Ti). In the case of Zr coating, a higher value of $L_{c2} = 14.8$ N is obtained. Next, together with increasing load force, complete break of the coating occurs. For Ti and Zr coating, critical load values L_{c3} occur at values higher than 30 N, which indicates the excellent adhesion strength on 316L stainless steel. In all coatings, the cohesive spallation is evident along the scratch track borders.

The contact angle goniometry results used to evaluate the wettability, water and diiodomethane wetting angles, and calculated SFE are shown in Table 6. Additionally, examples of drops placed on all tested samples' surface are presented in Fig. 8. The obtained results show significant differences in the value of water contact angle depending on the surface preparation methods. The lowest water wetting angle values are observed for the uncoated samples and samples with pure HAp coating, and the mean value for both coatings is $\theta_w \approx 76°$. The contact angle less than 90° suggested the hydrophilic character of the surface. Deposited Ti and Zr coatings on 316L base material change the character of the surface from hydrophilic to hydrophobic, and the mean values are similar $\theta_w \approx 115 - 118°$. Moreover, no significant changes in the wetting angle are observed for deposition HAp coating on Ti layer (Ti/HAp) and Zr layer (Zr/HAp) coatings ($\theta_w \approx 118°$). Only samples with Ti coating display greater affinity to polar groups of SFE than to polar ones. This is associated with the almost twofold lower value of diiodomethane contact angle obtained for Ti coating ($\theta_d \approx 25°$) compared to the other tested groups ($\theta_d = 44 - 51°$).

The open circuit potential E_{OCP} diagram of uncoated 316L stainless steel and studied coatings after exposure time of 1 h, in 7.4 pH of Ringer solution is shown in Fig. 9.

Specifically, for samples with Ti coating, E_{OCP} values begin to increase and then gradually stabilize. In the case of the other coatings investigated, E_{OCP} values first tend to shift toward more electropositive values and then suddenly decrease. An increase of E_{OCP} value and gradual stabilization indicate increased compactness passive layer or corrosion products on the samples overtime. Reduced E_{OCP} value indicates possible dissolution of the material surface. Additionally, for the Zr coating, after the value decreases, another increase of the potential to the mean

Table 6 Results of contact angle measurements and calculated SFE

No.	Coating	Wetting angle [°]		Surface free energy [mJ/m^2]		
		Distilled water	Diiodomethane	γ_S	γ_d^S	γ_p^S
1.	316L (substrate)	75.6 ± 3.7	51.2 ± 2.4	37.7	25.2	9.6
2.	316L_HAp	75.6 ± 2.7	46.4 ± 2.3	36.8	25.6	8.23
3.	316L_Ti	118.4 ± 2.1	25.1 ± 2.8	65.1	17.3	49.2
4.	316L_Zr	115.3 ± 2.5	44.2 ± 4.7	50.9	53.4	3.5
5.	316L_Ti/HAp	117.8 ± 3.8	46.2 ± 2.1	51.2	52.1	2.7
6.	316L_Zr/HAp	118.2 ± 1.2	48.3 ± 1.6	52.2	53.1	3.1

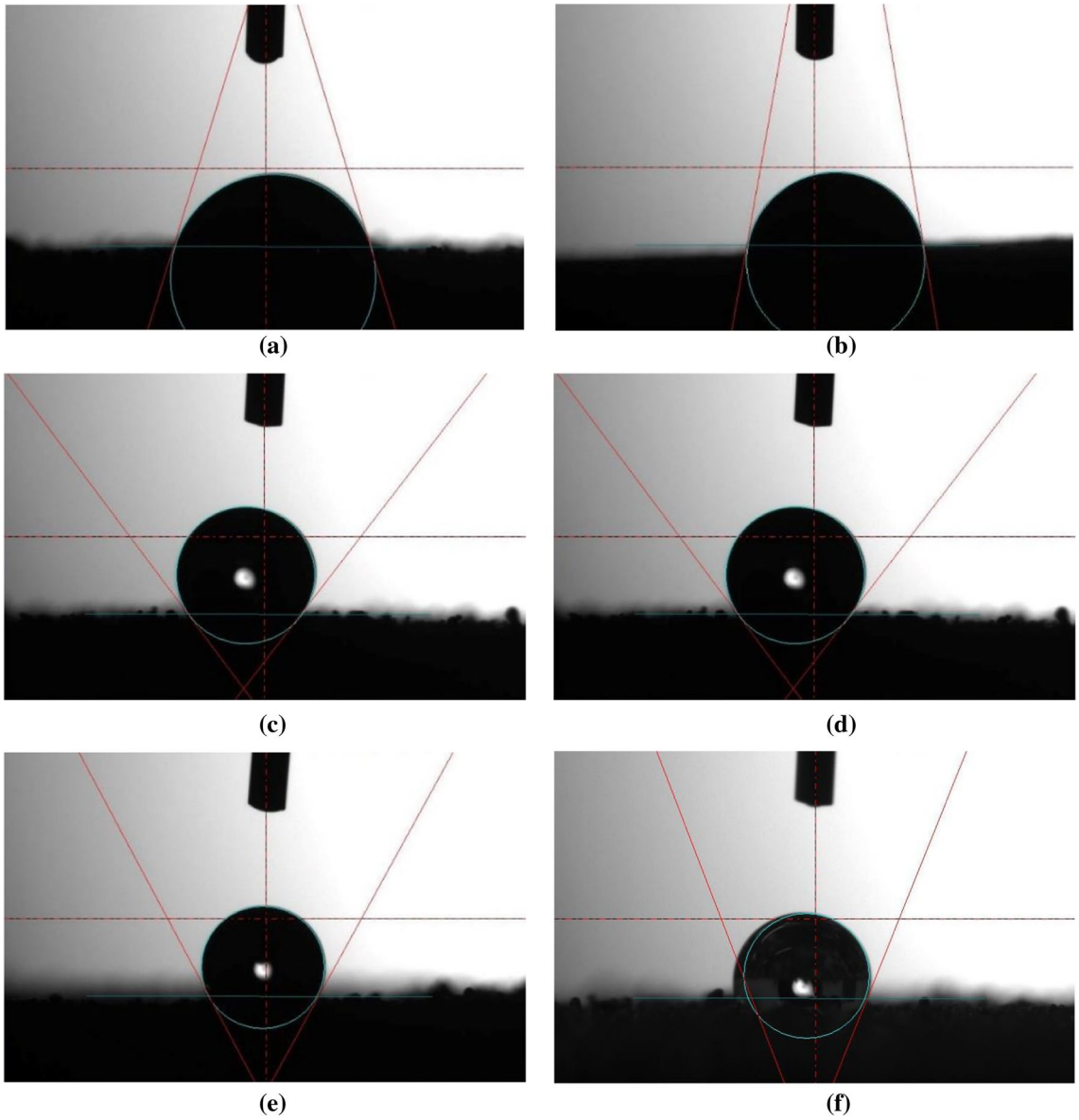

Fig. 8 Results of contact angle measurements: **a** drop unacted samples; **b** drop HAp coating; **c** drop Zr coating; **d** drop Ti coating; **e** drop Ti/HAp coating; **f** drop Zr/HAp coating

value is observed, which suggests local changes on the surface. E_{OCP} potential of Ti shows almost no change over the exposure time. The highest E_{OCP} value is obtained for samples with Zr coating, with mean value close to − 50 $mV_{Ag/AgCl}$ (corresponding to approx. + 149 mV_{NEH}), which belongs to the domains of the passive region in the Pourbaix diagram [42]. However, the registered oscillations can be associated with instability of the formed zirconium oxide (ZrO_2) layer under the test conditions. In general, ZrO_2 coatings are inhomogeneous and in this case should stabilize via addition of a different oxide, for example Y_2O_3 [43]. Additionally, the thin ZrO_2 passivation layer formed on the Zr coating surface is more efficient than TiO_2, developed on the Ti coating surface, which is also confirmed by the measured values. The mean value of E_{OCP} for Ti coating is − 325 $mV_{Ag/AgCl}$ (− 126 mV_{NEH}), which is the lowest value in the tested coatings group and corresponds to previous reports [31]. However, the obtained results for samples with Ti layer indicate that under steady-state conditions, the alloys form an oxide layer of TiO_2. The reference samples (uncoated) exhibit lower E_{OCP} potential compared to the coated samples.

The pitting corrosion test results in the form of anodic polarization curves are presented in Fig. 10, and the characteristic values, which describes corrosion resistance behavior of the tested coatings, are given in Table 7.

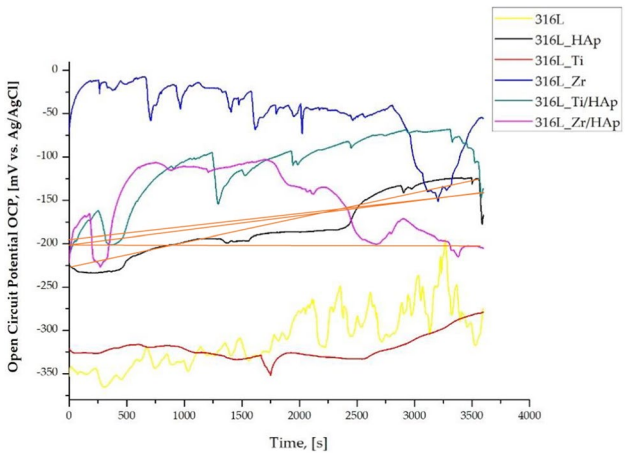

Fig. 9 The open circuit potential in Ringer solution of 316L substrate material and studied coatings: HAp, Ti, Zr, Ti/HAp, Zr/HAp, exposure time 1 h

Based on the pitting corrosion results, it is known that all tested coatings exhibit similar corrosion mechanisms. Additionally, all tested sample's anodic slope is similar to the cathodic slope (similar values of b_a and b_c are obtained), which suggests that the kinetics relates to the electrons transfer and the number and nature of electrons involved in both reactions (anodic and cathodic). Their hysteresis loops and the existence of breakdown potential have been recorded and the voltammetric curves show active to passive transition with current densities of approx. − 300 μA/cm^2. Samples with Ti layer (Ti and Ti/HAp coatings) and HAp coating display a plateau region from − 200 to + 100 mV and − 250 to + 100 mV, respectively, followed by a steady increase of current density. For uncoated stainless steel (316L), the mean value of corrosion resistance and breakdown potential are $E_{corr} = -285$ mV and $E_b = 322$ mV, respectively. Deposited porous coatings by APS process, excluding Ti-containing coatings (Ti and Ti/HAp), show a positive increase in the corrosion resistance value E_{corr} and breakdown potential E_b, while reduction of current density i_{corr} value is observed, which favorably affects the corrosion resistance. Generally, two distinct features of corrosion resistance coatings include high value of corrosion potential E_{corr} and low value of corrosion current density, which are determined from the intersection of fits of the anodic and cathodic branches of the log (current density) vs. potential plot to the Tafel equation. Corrosion potentials E_{corr} are the thermodynamic value, while current density i_{corr} is the kinetic value. The high corrosion potential is more favorable, but it can show only corrosion tendency. The corrosion rate is proportional to the current density i_{corr}. The highest values of corrosion potential are obtained for samples with Zr coating, with mean values of $E_{corr} = -85$ mV. Zr-coated samples also possess low value of current density $i_{corr} = 0.076$ μA/cm^2. Moreover, satisfactory corrosion resistance parameters are obtained for samples with Zr/Hap, with mean values of corrosion resistance $E_{corr} = -228$ mV and corrosion current resistance $i_{corr} = 0.06$ μA/cm^2. A similar tendency is obtained for samples with HAp coating, where $E_{corr} = -228$ mV and $i_{corr} = 0.05$ μA/cm^2. Enhanced corrosion behavior can be associated with low value of coatings porosity P (calculated based on corrosion resistance parameters), which is less than 8% for each sample and the values of protective efficiency coefficient of the coatings with Zr and HAp (pure Zr, HAp and Zr/HAp) show decisively higher values $P_e > 60\%$.

Samples with Ti and Ti/HAp coating are characterized by lower corrosion resistance, which confirmed the higher values of current density ($i_{corr} = 0.166$ μA/cm^2 and $i_{corr} = 0.216$ μA/cm^2, respectively), indicating the highest rate of corrosion. In the case of Ti or Ti/HAp coatings, the values of protective efficiency coefficient show mean values of $P_e = 8\%$ and $P_e = -10\%$, respectively. This can be attributed to high porosity ($P = 17\%$ for Ti samples and $P = 31\%$ for Ti/HAp samples) and loosely packed morphology with defects in the form of cracks, visible from the cross-sectional microscopic analysis (Fig. 3) [44]. Moreover, this can lead to the electrolyte permeating into the film, resulting in a large electroactive surface and high corrosion rate. Additionally, based on the observations, it can be concluded that the application of HAp coating to the previously deposited Ti coating may result in improved corrosion resistance.

To evaluate the corrosion properties, EIS measurements were performed. Impedance spectra of substrate 316L stainless steel with different coatings were recorded and presented in the form of Nyquist plot and Bode diagram (Fig. 11).

Figure 12 shows the impedance spectra determined during the EIS test, fitted using the equivalent electrical circuit (EEC). EEC was fitted using EC-lab software from Bio-Logic. The individual elements are as follow: R_s—resistance of the Ringer solution, where the tests were carried out, R_{pore}—resistance between the electrolyte and the double layer of the material, CPE_{dl}—constant phase element of non-uniformity of electrochemical properties of the material surface (capacity of the double layer porous surface), R_{ct}—determines the charge transfer resistance in the electrolyte in the zone near the material (resistance of the passive film), W—Warburg impedance representing the process of diffusion of reagents. The mathematical impedance (Z) model of the above system is presented in Eq. (3).

$$Z = R_s + \frac{Y(j^{\omega})a_1}{R_{pore} + \frac{R_{ct}}{W}}. \tag{3}$$

In the performed investigations, the value of electrolyte resistance is registered at the level of 1 ÷ 46 Ω, the coefficient

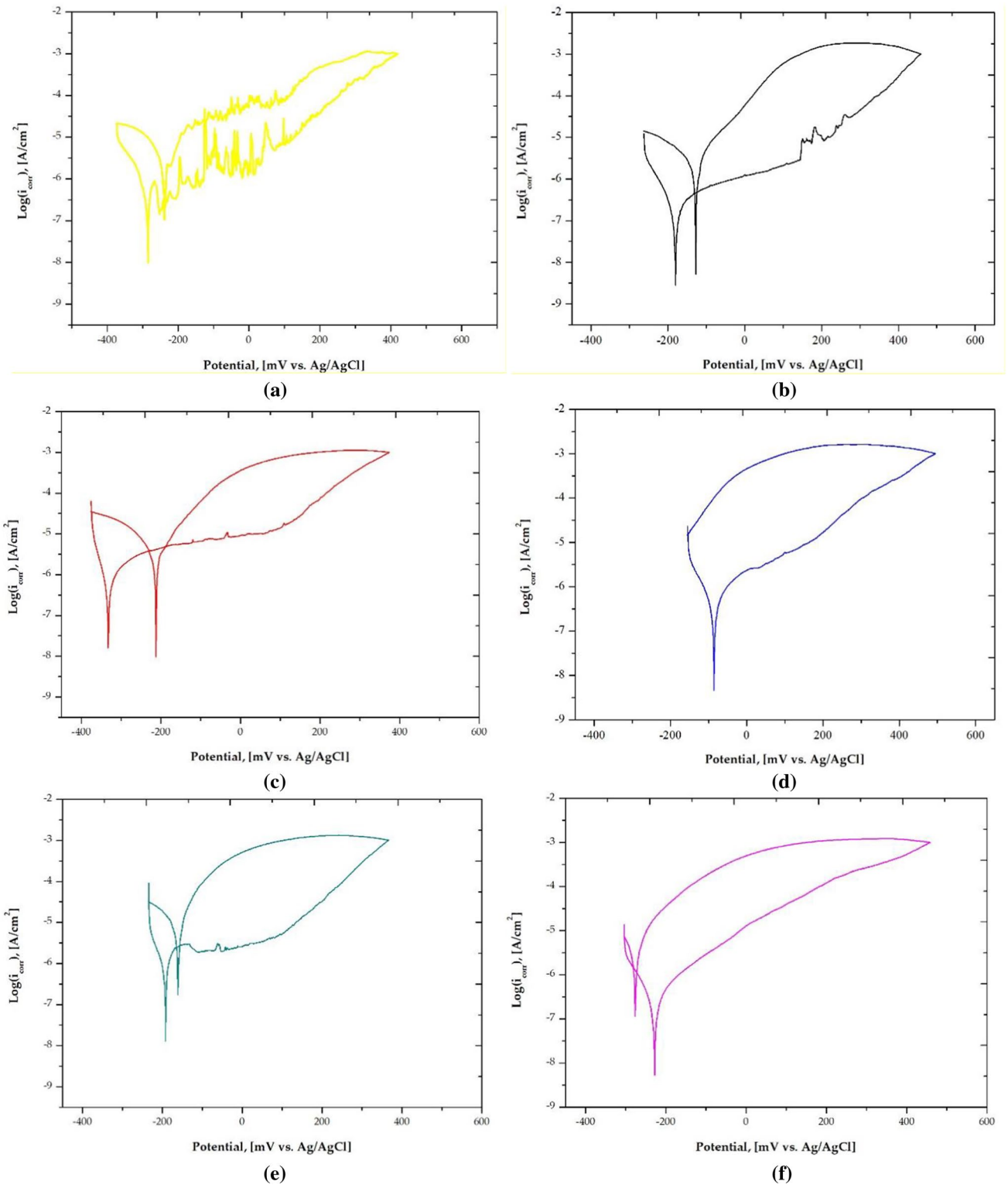

Fig. 10 The polarization curves of tested samples: **a** substrate material 316L; **b** HAp coating; **c** Ti coating; **d** Zr coating, **e** Ti/HAp coating; **f** Zr/HAp coating

Table 7 Results of pitting corrosion test—mean values and standard deviations

No.	Coating	E_{corr} [mV]	E_b [mV]	b_a [mV]	b_c [mV]	R_p [kΩ ·cm^2]	i_{corr} [μA/cm^2]	P [%]	P_e [%]
1.	316L	− 285	322	18	24	27	0.18	–	–
2.	HAp	− 180	390	26	21	108	0.05	74	3.5
3.	Ti	− 333	274	20	15	22	0.16	7	17
4.	Zr	− 85	392	18	15	46	0.08	62	8
5.	Ti/Hap	− 191	294	11	14	12	0.20	− 12	31
6.	Zr/Hap	− 228	350	24	22	81	0.06	67	4.5

E_{corr} corrosion potential, E_b breakdown potential, b_a, b_c Tafel component, R_p polarization resistance, i_{corr} current corrosion density, P coatings porosity, P_e protective efficiency coefficient

of CPE1 element for the samples with HAp and Ti/HAp coatings assume the value of approximately 0.56, which may indicate the type of Warburg impedance type of interactions, whereas other materials display values above 0.8. This defines the type of element as capacitive. The Nyquist diagram shows that the curves are basically rectilinear throughout and at low frequencies suggest that the corrosion process is controlled by the diffusion of reactants and is characteristic of Warburg-type impedances. Zr/HAp sample exhibits the highest directional coefficient value, indicating the best resistance to the corrosive effects of the test environment. However, at high-frequency range up to 16 Hz, the lowest corrosion rate is recorded for Ti-coated sample and highest rate for Hap-coated sample over a very wide range from 100 kHz to 16 Hz. In the low-frequency range from 10 to 0.4 Hz, Ti/Hap-coated sample corrodes fastest. Furthermore, by comparing the corrosion rates based on the directional coefficients of the recorded curves in the very low-frequency range, Ti- and Zr-coated samples undergo the fastest corrosion.

As shown in Fig. 12, Zr/HAp coating is characterized by the highest impedance modulus of all samples tested, which is evident over almost the entire frequency range. At low-frequency range of 0.001 ÷ 0.1 Hz, Ti coating shows the lowest impedance, suggesting the lowest corrosion resistance, whereas at frequencies from 0.1 to 6300 Hz, the Ti/HAp sample exhibits the lowest impedance value, and the Ti and Zr samples show comparable corrosion resistance. At high frequencies, apart from the highest impedance of the Zr/Hap sample, comparable impedance values are registered for the other samples. It is also worth noting that the HAp sample in the high and very high-frequency range of 1 ÷ 100 kHz has the highest impedance value, greater than that of the Zr/HAp sample by between 6 and 42 Ωcm^2. Graphs of phase angle changes were also used to evaluate the corrosion properties, where the Ti sample had the highest values of − 83 ÷ − 77°, but only in a narrow frequency range (1 ÷ 10 kHz). The large value of the phase shift angle in the high-frequency region allows to define the features of the double layer between the solution and the substrate material as capacitive. However , a distinct reaching by the phase shift angle of a value close to zero and impedance values stabilizing and reaching close to zero relate to the substrate material's resistive character. The most stabilized value of the phase shift angle, in the widest range, from 2.5 to 6300 Hz, is for Zr/HAp sample (− 74 ÷ − 56°) and Zr sample (− 71 ÷ − 50°); in these frequency ranges, the impedance spectrum on the Bode diagram runs linearly, which may indicate good tightness of the applied coatings.

The characteristic parameters of the EIS test is presented in Table 8. The highest R_{ct} resistance value is obtained by samples with Zr/HAp coatings, and the mean value is 13 kΩ cm^2.

The composite coatings: HAp and Ti/HAp show significantly higher R_{pore} value in respect to other coatings. The R_{pore} parameter of EEC can be linked with porosity present on the surface of related coatings and entrapment of the electrolyte Ringer solution in such porosity, generating increased resistance. The above coatings show increased resistances of both electrolyte (R_s) and electrolyte in porosities, cavities, cracks and other surface defects (R_{pore}).

Therefore, the deposited composite coating Zr/HAp, which is characterized by good quality and compact structure, contributes to the improvement of anticorrosive properties.

SEM results after corrosion resistance tests and EDS analysis results of all studied coatings are presented in Fig. 13. Before the tests, the surface topography of the APS coating comprises porosities, macro- and microcracks and amorphous structures, which can provide focal corrosion points. After the corrosion test of all tested samples, excluding Zr coating, the formation of the sub-micron-scale pits are observed. Additionally, the formation of the apatite structure is observed. EDS analysis shows increased Ca, potassium and oxygen content, which confirms the apatite's growth. Furthermore, HAp coating promotes the formation of the apatite structure. Before the corrosion test, Ca/P ratio for HAp coatings is approximately 1.93, whereas after the test it is above 2. After immersion in Ringer solution, Ti and Zr coatings display Ca structure as a minor intensity, which is precipitated on the surface and non-homogeneously distributed over the entire Ti and Zr splats. Such results

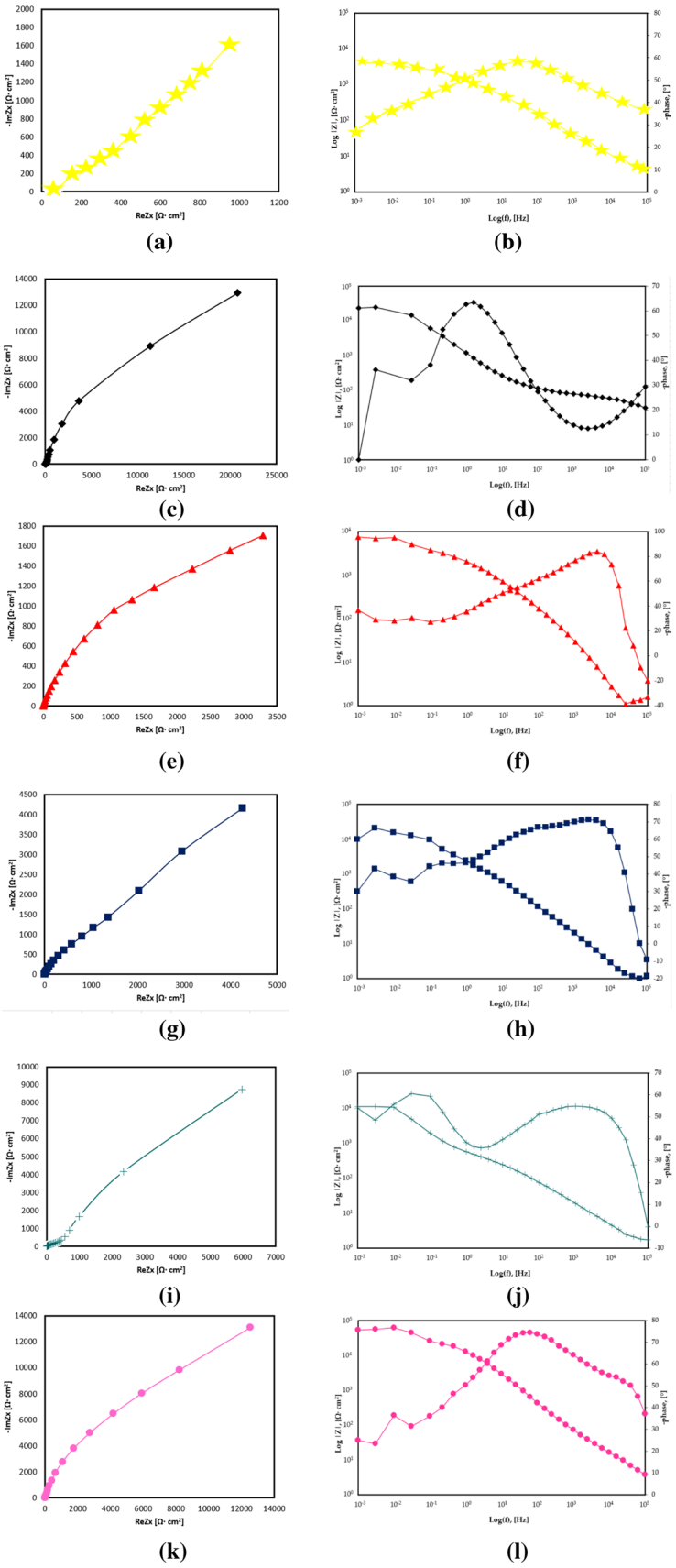

Fig. 11 Results of electrochemical impedance spectroscopy (EIS), the Nyquist on left and Bode diagram on the right: **a**, **b** substrate material 316L; **c**, **d** HAp coating; **e**, **f** Ti coating; **g**, **h** Zr coating; **i**, **j** Ti/HAp coating; **k**, **l** Zr/HAp coating

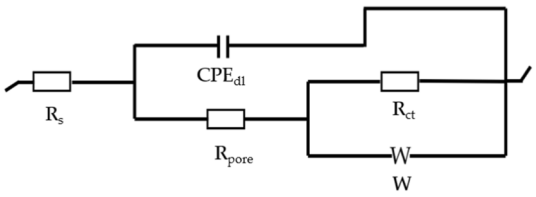

Fig. 12 Equivalent electrical circuit EEC of all tested samples

are attributed to high energy and rough surface. Similar results of plasma electrolytic oxidation (PEO) coating were observed by Aktuğ et al. [45]. For the composite coatings, Ti/HAp and Zr/HAp, a more significant apatite formation is observed.

4 Discussion

First, the quality of HAp, Ti, Zr, and their combination coatings deposited by the APS method was investigated. Based on microscopic observations, all coatings are characterized by heterogeneous morphology with many surface defects, i.e., pores and cracks. Additionally, the presence of partially melted spherical or ellipsoidal particles is detected. HAp coating has very poor cohesive bonding with the substrate material, which can be caused by the brittle nature of HAp. During APS process, HAp disintegrates at high temperatures into Ca and P, which forms on the base material porous structures and amorphous hump, resulting in weak interfacial bond. As a result, the coating may be damaged during the mechanical preparation of the cross-section samples. The poor interface bonding can also explain the presence of numerous micro- and macrocracks running across the surface of the plasma-sprayed HAp coatings. The process of microcracks formation can also be associated with the existence of high thermal stresses caused by rapid solidification (due to relative cooling of the electrolyte) of molten materials during APS process. The high solidification rate is associated with the solidification process of pure Hap, which involves cooling of single-phase with homogeneous thermal conductivity. The surface morphology of Ti and Zr coatings are very similar and characterized by the solidified splats with partially melted particles. In general, the splats' size and morphology depend on the interaction between the spray particles and substrate material, and the interaction is defined by the velocity of melted particles and their degree of melting. During APS process, particles of Ti and Zr wires melted by the plasma jet move toward the substrate. Before interaction with the base material, the particles are cooled down by moving the plasma jet to a lower temperature zone. Importantly, both Ti and Zr are characterized by a similar range of melting temperature and thermal conductivity ($T = 1668$ °C, $\lambda = 21.9$ W/mK and $T = 1855$ °C, $\lambda = 22.7$ W/mK, respectively). It is possible to correlate the particles' temperature and velocity before the collision to the substrate with the resultant structure and morphology of the coating. Based on the results, it can be determined that the size and thickness of the sprayed particles and degree of melting in the plasma jet can vary by spraying parameters [37], which are very similar for Ti and Zr coatings. For both coatings, the existence of cracks perpendicular and parallel to the coating/substrate interface are observed. It should be noted that Ti coatings exhibit more defects, including cracks, compared to the Zr surface. The perpendicular cracks are formed due to rapid cooling of the melted Ti and Zr particles, which collide on the substrate material or existing previously layer with the following spread. The solid surface confines the thermal shrinkage of the particle. In effect, in the coagulated particles, the quenching stress generates and becomes the tensile stress of the coating. The formation of vertical cracks leads to the release of internal stress and relaxing thermal stress. The composite coatings' morphology (Ti/HAp or Zr/HAp) shows a combined property of the component layers. Based on the results of the scratch test, Ti and Zr coatings are characterized by good adhesion to the substrate material 316L stainless steel. However, in the case of Zr coating, the first failure occurs at 14.8 N load, which indicates the best adhesion to the substrate in the tested group. The mechanical properties, including toughness of the coating and adhesion to the substrate material, represents an important asset in medical application, characterized by demanding conditions [44]. The high coating adhesion to the substrate guarantees high deformation resistance and load-bearing ability

Table 8 EIS analysis results

No.	Coatings	R_s [kΩcm^2]	CPE$_{dl}$		R_{pore} [kΩcm^2]	R_{Ct} [kΩcm^2]	s_3 [Ωs$^{-1/2}$]
			Y_1 [Ω cm^{-m} s^{-n}]	a_1			
1.	316L	0.001	25.83e−6	0.90	0.06	10.40	4929
2.	316L_HAp	46.00	0.375e−3	0.57	53.00	47.00	2.5
3.	316L_Ti	0.80	24.18e−6	0.85	1.00	20.70	1743
4.	316L_Zr	0.70	12.63e−6	0.91	0.02	64.00	2975
5.	316L_Ti/HAp	0.60	0.522e−3	0.56	48.00	0.95	2
6.	316L_Zr/HAp	4.20	7.118e−6	0.34	0.07	136.00	25,900

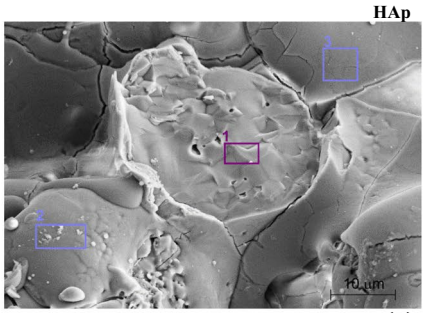

Point	Elements, wt. [%]		
	Ca	P	O
1.	34	16	41
2.	35	17	34
3.	34	16	16

Point	Elements, wt. [%]		
	Ti	O	Ca
1.	71	21	12
2.	67	2	10
3.	59	21	15

Point	Elements, wt. [%]		
	Zr	O	Ca
1.	78	11	11
2.	79	8	12

Point	Elements, wt. [%]			
	Ti	Ca	P	O
1.	57	-	-	27
2.	-	28	-	34
3.	-	35	16	37

Point	Elements, wt. [%]			
	Zr	Ca	P	O
1.	-	71	5	23
2.	-	44	12	17
3.	2	30	17	34

Fig. 13 SEM results and EDS analysis of: **a** substrate material 316L; **b** HAp coating; **c** Ti coating; **d** Zr coating; **e** Ti/HAp coating; **f** Zr/HAp coating

of the system can effectively increase the tribological and anticorrosive characteristics [46, 47]. Generally, the coating adhesion on the substrate is conditioned by physical and chemical bonding, and mechanical interlock. Physical and chemical bonding is determined by material composition, and mechanical interlock is associated with the substrate materials roughness. For this purpose after coating deposition, the sandblasted process is performed. Miletica et al. [48] found that the formation of the first adhesion failure (L_{c1}) is hindered when a great amount of plastic deformation is needed, and the rough surfaces with asperities require more energy for getting plastically deformed. For all tested coatings, only L_{c2} and L_{c3} failures are observed. However, the beneficial effect of sputtering Ti and Zr layers on Hap binding is demonstrated. The discussed morphological elements of the studied coating show expected surface features typical of plasma-sprayed coatings. Similar results were obtained by Aktuğ et al. [45] and Shang et al. [49], where the surface topography, especially the surface roughness of tested samples, plays a significant role in the wettability phenomena. The surface roughness measurements show that the samples with Ti or Zr coating are characterized by close to fourfold higher values of R_a parameters compared to the substrate material (316L) and HAp coating. As previously mentioned, the surface morphology of samples in the initial state (316L) and with HAp coating is rough, while the presence of evenly distributed splats characterizes the surface morphology of Ti and Zr coatings. When a drop of polar liquid (water) is placed on a rough surface, two wetting states can occur (Fig. 14)—Wenzel state (the polar liquid drop penetrates downward into the roughness to establish perfect liquid–solid contact) and Cassie–Baxter state (the polar liquid drop is suspended on the peaks of roughness) [50, 51].

Both Wenzel and Cassie–Baxter states can exhibit high wetting angle. However, in the case of Wenzel state, the movement of the drop requires a large external force due to the extensive contact between the liquid drop and solid, which is caused by strong adhesion of the liquid drop to the rough surface. In effect, the penetrated liquid portion of Wenzel state produces a high contact angle hysteresis, which

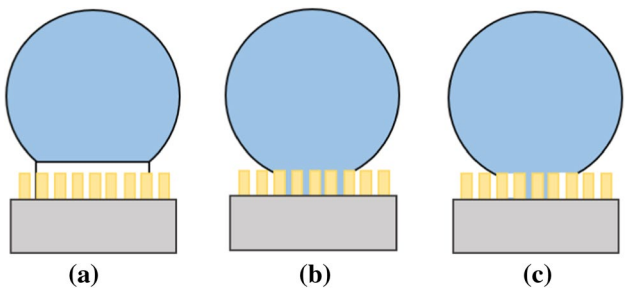

Fig. 14 Schematic of a measured liquid drop under **a** Wenzel state; **b** Cassie–Baxter state; **c** partial Cassie–Baxter state

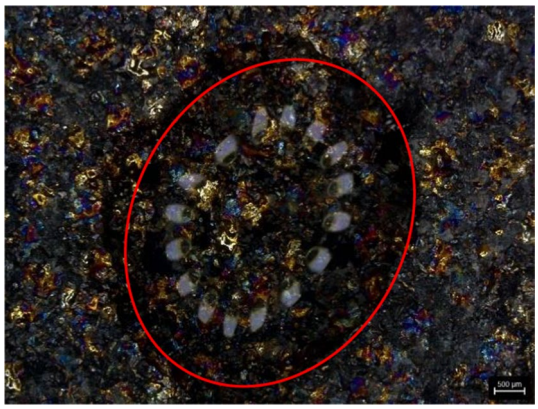

Fig. 15 Schematic of a measured liquid drop. Below, shape of the drop

can be observed for the samples with Ti and Zr coatings (Fig. 15). The deposition of HAp coatings on the surface of Ti and Zr samples displays no significant change to the surface wetting state due to the exact mapping of the surface topography.

According to literature data, the surface morphology and topography also affect the corrosion behavior and bioactivity of biomaterials [52, 53]. The topographical changes—roughness and pores, can provide focal corrosion points, but also points for protein and cells attachment, as well as contributing to apatite formation on coatings' surfaces. Electrochemical tests show that Zr and Zr/HAp coatings are characterized by optimum corrosion resistance. OCP measurements reveal that both sample groups doped with Zr exhibit more positive E_{OCP} values compared to other samples. According to the results obtained by Dai et al. [54], the shift of OCP potential in the more noble direction suggests the formation of a passive layer, which is considered the corrosion protective barrier. Additionally, the results of potentiodynamic test and EIS analysis confirm the interpretation of OCP behavior, due to the highest values of breakdown potential E_b and charge transfer resistance R_{ct}, and the lowest values of current density i_{corr} obtained for the Zr and Zr/HAp samples. The high values of charge transfer resistance R_{ct} suggest that Zr and Zr/Hap display high electrochemical stability. Based on the porosity calculation from the potentiodynamic test, Zr coating possesses the lowest porosity, hence, resulting in higher anti-corrosion properties. Additionally, the results of the corrosion test and porosity calculation correspond to the results of coating adhesion to the substrate material. Zr coating exhibits higher values of L_c parameters ($L_{c2} = 14.8$ N and $L_{c3} > 30$ N). HAp and Ti-containing coatings (Ti and Ti/HAp) have more defective structures. Pores do not provide sufficient resistance to coating failure propagation, which results in lower

corrosion properties. After the corrosion test of all tested samples, excluding those with Zr coatings, the formation of sub-micron-scale pits is observed, which is attributed to the dissolution and, in effect, the premature failure of the APS layers in the corrosive medium. According to the results presented by Ramachandran et al. [55], the corrosion behavior may be associated with wettability and surface free energy (SFE). The rate of corrosion reactions on the hydrophobic surface can be expressed by Eq. (4), where r_0 is the rate of corrosion reaction under ideal surface conditions, R is the roughness ratio, T is the absolute temperature, γ is the surface free energy, and $0 \leq f_{SL} \leq 1$ is the fractional solid–liquid interfacial area:

$$r = r_0 \exp\left(\frac{\gamma_A(1 - f_{SL})}{RT}\right). \tag{4}$$

Ramachadran et al. [55] and Akaltun et al. [56] showed that increased corrosion resistance is due to decreased corrosion current with increasing water contact angle and surface free energy. Similar trends have been reported via thin ZnO layer deposition by the atomic layer deposition (ALD) method, which is characterized by the developed surface roughness on nanoscale [31]. Additionally, for all studied coatings after immersion in corrosion solution, the formation of apatite structure is also observed, which was confirmed by EDS analysis—the increased presence of Ca, P and O. In general, the HAp structure promotes the formation of the apatite structure—after the corrosion test in Ringer solution, Ca/P ratio increases from 1.93 to above 2. In the case of Ti and Zr coatings, the formation of slight forms of Ca structure is noted. The pores on the surface benefit apatite structure formation. Ti/HAp and Zr/HAp coatings display the greatest increase in the presence of apatite structures. Hence, the apatite structure can be preferentially formed on defect regions. The results obtained by Stalder et al. [57] confirm that samples with high surface free energy (SFE) is more adhesive than those with low surface free energy. Therefore, samples exhibiting a hydrophilic character of the surface and low SFE (uncoated 316L) have lower bioactivity after immersion in Ringer solution SBF. Han et al. [58] shows that it is possible for this sample group to have greater cell attachment capabilities. After the corrosion test in the Ringer solution, P atoms on HAp coatings increase the ionic activity between the surface and corrosion medium. In the first step, PO_4^{3-} ions are formed on the surface. Next, under corrosion conditions, Ca^{2+} ions, which are positively charged, migrate into negatively charged PO_4^3, and the coating's surface becomes positively charged. To obtain charged homeostasis on the coating's surface, PO_4^{3-} ions must migrate to the surface. In effect, Ca^2 and PO_4^3 ions react and supersaturation of the surface of Ca and P occurs. Subsequently, the apatite structures spontaneously grow through the coating's surface.

5 Conclusions

The main conclusions derived from the presented research of APS coating properties on 316L stainless steel substrate are summarized as follows:

- The studied coatings show typical morphology of the APS process, where porosities and cracks are observed. Pure HAp coating exhibits poor cohesive bonding with the 316L substrate material. The introduction of Ti and Zr interlayer under the HAp top layer improves the surface morphology and further surface properties. The morphology of the Ti and Zr layer is similar and indicates that dominant factors influencing their nature are the parameters of APS deposition process. Ti coating shows more defects compared to Zr coating. The top surface morphology of composite coatings Ti/HAp and Zr/HAp is less defective than the coating surface with a single HAp layer. Pure Ti and Zn coating shows higher surface roughness, when compared to pure HAp coating, while composite coating Ti/HAp and Zr/HAp shows reduced roughness due to partial filling of the spaces between splats on the surface. The use of HAp as a top layer on the surface of previously deposited Ti or Zr layers leads to stronger bonding of Hap to the surface, because of a more developed surface of the layers.
- The coatings containing HAp (HAp, Zr/HAp, Ti/HAp) show Ca/P ratio in range of $1.8 \div 1.9$, which is higher than the stoichiometric HAp (1.67) value. This may positively influence the differentiation of osteogenic cells; thus, good adhesion to the bones can be expected for potential implant application.
- The stainless steel substrate material as well as pure HAp coating shows hydrophilic character, while deposition of pure Ti and Zr as well as composite coatings (Ti/HAp and Zr/HAp) changes its character to hydrophobic. The surface wetting properties are not significantly changed compared to pure coating with interlayer of Ti and Zr and composite coatings (Ti/HAp and Zr/HAp) due to the exact mapping of the surface topography by the top HAp layer.
- Considering the adhesion of coatings to 316L, the substrate evaluated in the scratch test, the Hap-type coating shows lower adhesion (complete brake 13.5 N) than Zr or Ti-type coating (complete break > 30 N).
- The coated stainless steel surface shows E_{OCP} in Ringer solution in the following order, from most positive to the most negative values: Zr < Ti/Hap < HAp < Zr/Hap < Ti coating. Except for the base material and Ti coating,

other coatings show decreased E_{OCP} values during immersion and fluctuations to more negative and positive regions, while the final values are close to the initial one. Increased E_{OCP} value may be related to increased compactness of the passive layer and corrosion products on the surface with time, while decreased E_{OCP} value indicates possible dissolution of the material surface. Thus, in tested coating, the continuous process of the surface layer reforming is present and relates to local changes on the surface.

- The pitting corrosion resistance based on Tafel analysis shows that optimal electrochemical parameters are obtained for pure Zr coatings—low corrosion current density (i_{corr}), high corrosion potential E_{corr} and breakdown E_b potential. Zr/HAp and HAp coatings exhibit good corrosion resistance. To precisely evaluate electrochemical behaviors, the protective efficiency P_e factor is introduced to determine the relationship between corrosion current density of the coating and substrate material. The protective efficiency P_e of the coatings is in the following order (from the highest): Zr < Zr/Hap < Ti < Ti/HAp, while Zr and Zr/HAp coating show $P_e > 60\%$, close to uncoated substrate ($P_e > 70\%$), and Ti and Ti/HAp only possess $P_e = 8\%$ and $P_e = 20\%$, respectively. Therefore, the pitting corrosion resistance of the tested coatings is the highest for the variants with Zr (Zr and Zr/HAp coatings).
- EIS analysis also confirms that the best protective properties in the Ringer solution is observed for Zr/HAp coatings, characterized by high charge transfer resistance R_{ct}, related to increased surface passivity and implicitly of the resistance against the corrosion, resulting in high electrochemical stability. HAp, Ti, and Ti/HAp coatings show more defective structure—high R_{pore} parameter linked with porosity and other surface defects present on the surface and entrapment of the electrolyte solution in such areas.

Author contributions All authors contributed to the study conception and design. Material preparation, data collection and analysis were performed by AW, ZB, MA, SV, OK, SK and MB. The first draft of the manuscript was written by AW, ŁR, MS and OB and all authors commented on previous versions of the manuscript. All authors read and approved the final manuscript.

Funding This study received great support from the EU-project H2020-MSCA-RISE-2018 Number 823786, i-Weld.

Availability of data and material The data that support the findings of this study are available from the corresponding author [Anna Woźniak], upon reasonable request.

Code availability All data generated or analyzed during this study are included in this published article.

Declarations

Conflict of interest The authors declare that they have no conflict of interest.

Ethics approval Not applicable.

References

1. Branemark PI, Zarb GAAT. Tissue—integrated prostheses. Chicago: Quintessen; 1985.
2. Kamachimudali U, Sridhar TM, Raj B. Corrosion of bio implants. Sadhana. 2003;28:601–37.
3. Evans EM, Freeman MAR, Miller AJ, Vernon-Roberts B. Metal sensitivity as a cause of bone necrosis and loosening of the prosthesis in total joint replacement. J Bone Jt Sur Br. 1974;56-B:626–42.
4. Gilbert JL. Corrosion in the human body: metallic implants in the complex body environment. Corrosion. 2017;73:1478–95.
5. Zhao T, Mu G. The adsorption and corrosion inhibition of anion surfactants on aluminium surface in hydrochloric acid. Corros Sci. 1999;41:1937–44.
6. Alcázar JCB, Lemos RMJ, Conde MCM, Chisini LA, Salas MMS, Noremberg BS, et al. Preparation, characterization, and biocompatibility of different metal oxide/PEG-based hybrid coating synthesized by sol–gel dip coating method for surface modification of titanium. Prog Org Coat. 2019;130:206–13.
7. Hayajneh MT, Almomani M, Al-Daraghmeh M. Enhancement the corrosion resistance of AISI 304 stainless steel by nanocomposite gelatin–titanium dioxide coatings. Manuf Technol. 2019;19:759–66.
8. Cordova LA, Stresing V, Gobin B, Rosset P, Passuti N, Gouin F, et al. Orthopaedic implant failure: aseptic implant loosening—the contribution and future challenges of mouse models in translational research. Clin Sci. 2014;127:277–93.
9. O'Neill E, Awale G, Daneshmandi L, Umerah O, Lo KW-H. The roles of ions on bone regeneration. Drug Discov Today. 2018;23:879–90.
10. Woźniak A, Adamiak M, Chladek G, Bonek M, Walke W, Bialas O. The influence of hybrid surface modification on the selected properties of CP titanium grade II manufactured by selective laser melting. Materials. 2020;13:2829.
11. Bialas O, Lis M, Woźniak A, Adamiak M. Laser superficial fusion of gold nanoparticles with PEEK polymer for cardiovascular application. Materials. 2021;14:971.

12. Williams DF. The *Williams* dictionary of biomaterials. Liverpool: Liverpool University Press; 2011.
13. Singh S, Prakash C, Singh H. Deposition of HA-TiO_2 by plasma spray on β-phase $Ti_{-35}Nb_{-7}Ta_{-5}Zr$ alloy for hip stem: characterization, mechanical properties, corrosion, and in-vitro bioactivity. Surf Coat Technol. 2020;398:126072.
14. Lv H, Zhao W, An Q, Nie P, Wang J, Chu PK. Nanomechanical properties and microstructure of ZrO_2/Al_2O_3 plasma sprayed coatings. Mater Sci Eng A. 2009;518:185–9.
15. Cao J, Lian R, Jiang X. Magnesium and fluoride doped hydroxyapatite coatings grown by pulsed laser deposition for promoting titanium implant cytocompatibility. Appl Surf Sci. 2020;515:146069.
16. Pham DQ, Berndt CC, Gbureck U, Zreiqat H, Truong VK, Ang ASM. Mechanical and chemical properties of Baghdadite coatings manufactured by atmospheric plasma spraying. Surf Coat Technol. 2019;378:124945.
17. Lu J, Rao MP, MacDonald NC, Khang D, Webster TJ. Improved endothelial cell adhesion and proliferation on patterned titanium surfaces with rationally designed, micrometer to nanometer features. Acta Biomater. 2008;4:192–201.
18. Meinert K, Uerpmann C, Matschullat J, Wolf GK. Corrosion and leaching of silver doped ceramic IBAD coatings on SS 316L under simulated physiological conditions. Surf Coat Technol. 1998;103–104:58–65.
19. Ding Q, Zhang X, Huang Y, Yan Y, Pang X. In vitro cytocompatibility and corrosion resistance of zinc-doped hydroxyapatite coatings on a titanium substrate. J Mater Sci. 2015;50:189–202.
20. Furuzono T, Okazaki M, Azuma Y, Iwasaki M, Kogai Y, Sawa Y. Newly developed biocompatible material: dispersible titanium-doped hydroxyapatite nanoparticles suitable for antibacterial coating on intravascular catheters. In: Kawanishi H, Takemoto Y, editors. Contributions to nephrology [Internet]. S. Karger AG; 2017 [cited 2021 Mar 9]. p. 144–52. Available from: https://www.karger.com/Article/FullText/450744.
21. Melero HC, Sakai RT, Vignatti CA, Benedetti AV, Fernández J, Guilemany JM, et al. Corrosion resistance evaluation of HVOF produced hydroxyapatite and TiO_2-hydroxyapatite coatings in Hanks' solution. Mat Res [Internet]. 2018 [cited 2021 Jul 4];21. Available from: http://www.scielo.br/scielo.php?script=sci_arttext&pid=S1516-14392018000205105&lng=en&tlng=en.
22. Zhao X, Niinomi M, Nakai M, Ishimoto T, Nakano T. Development of high Zr-containing Ti-based alloys with low Young's modulus for use in removable implants. Mater Sci Eng C. 2011;31:1436–44.
23. AlFarraj AA, Sukumaran A, Al Amri MD, Van Oirschot AB, Jansen JA. A comparative study of the bone contact to zirconium and titanium implants after 8 weeks of implantation in rabbit femoral condyles. Odontology. 2018;106:37–44.
24. Thakare JG, Pandey C, Mulik RS, Mahapatra MM. Mechanical property evaluation of carbon nanotubes reinforced plasma sprayed YSZ-alumina composite coating. Ceram Int. 2018;44:6980–9.
25. Thakare JG, Mulik RS, Mahapatra MM. Effect of carbon nanotubes and aluminum oxide on the properties of a plasma sprayed thermal barrier coating. Ceram Int. 2018;44:438–51.
26 Alontseva D, Ghassemieh E, Voinarovych S, Kyslytsia O, Polovetskyi Y, Prokhorenkova N, et al. Manufacturing and characterisation of robot assisted microplasma multilayer coating of titanium implants: Biocompatible coatings for medical implants with improved density and crystallinity. Johnson Matthey Technol Rev. 2020;64:180–91.
27. de Vasconcellos LMR, Leite DO, de Oliveira FN, Carvalho YR, Cairo CAA. Evaluation of bone ingrowth into porous titanium implant: histomorphometric analysis in rabbits. Braz Oral Res. 2010;24:399–405.
28. Dorozhkin S V. Calcium orthophosphate deposits: preparation, properties and biomedical applications. Mater Sci Eng C 2015:272–326.
29. Seah KHW, Thampuran R, Teoh SH. The influence of pore morphology on corrosion. Corros Sci. 1998;40:547–56.
30. PN EN ISO 5832-9:2007. Implants for surgery—metallic materials—Part 9: wrought high nitrogen stainless steel. Geneva, Switzerland, 2017.
31. Woźniak A, Walke W, Jakóbik-Kolon A, Ziębowicz B, Brytan Z, Adamiak M. The influence of ZnO oxide layer on the physicochemical behavior of Ti_6Al_4V titanium alloy. Materials. 2021;14:230.
32. PN-EN ISO 17475:2010. Corrosion of metal and alloys—electrochemical test methods—guidelines for conducting potentiostatic and potentiodynamic, polarization measurements. Geneva: ISO. p. 201.
33. Nozawa K, Aramaki K. One- and two-dimensional polymer films of modified alkanethiol monolayers for preventing iron from corrosion. Corros Sci. 1999;41:57–73.
34. Elsener B, Rota A, Böhni H. Impedance study on the corrosion of PVD and CVD titanium nitride coatings. Mater Sci. 1991;44–45:29–38.
35. Vladescu A, Pruna V, Kulesza S, Braic V, Titorencu I, Bramowicz M, et al. Influence of Ti, Zr or Nb carbide adhesion layers on the adhesion, corrosion resistance and cell proliferation of titania doped hydroxyapatite to the Ti6Al4V alloy substrate, utilizable for orthopaedic implants. Ceram Int. 2019;45:1710–23.
36. Fauchais P. Understanding plasma spraying. J Phys D Appl Phys 2004:R86.
37. Kumari R, Majumdar JD. Microstructure and surface mechanical properties of plasma spray deposited and post spray heat treated hydroxyapatite (HA) based composite coating on titanium alloy ($Ti-_6Al-_4V$) substrate. Mater Charact. 2017;131:12–20.
38. Shinde SV, Gildersleeve VEJ, Johnson CA, Sampath S. Segmentation crack formation dynamics during air plasma spraying of zirconia. Acta Mater. 2020;183:196–206.
39. Mifune N, Harada Y. Mechanism of vertical microcracking in $CaO{\cdot}SiO_2$–$CaO{\cdot}ZrO_2$ sprayed thermal barrier top coating.
40. Jeong J, Kim JH, Shim JH, Hwang NS, Heo CY. Bioactive calcium phosphate materials and applications in bone regeneration. Biomater Res 2019:1–11.
41 Eliaz N, Metoki N. Calcium phosphate bioceramics: A review of their history, structure, properties, coating technologies and biomedical applications. Materials. 2017;10:334.
42. Edström C. Wet etching of optical thin films. Undefined. 2010.
43. Ziębowicz A, Woźniak A, Ziębowicz B, Kosiel K, Chladek G. The effect of atomic layer deposition of ZrO_2 on the physicochemical properties of cobalt based alloys intended for prosthetic dentistry. Arch Metall Mater. 2018;63:1077–82.
44. Musil J, Jirout M. Toughness of hard nanostructured ceramic thin films. Surf Coat Technol. 2007;201:5148–52.
45. Aktuğ SL, Durdu S, Yalçın E, Çavuşoğlu K, Usta M. In vitro properties of bioceramic coatings produced on zirconium by plasma electrolytic oxidation. Surf Coat Technol. 2017;324:129–39.
46. Ou YX, Lin J, Che HL, Sproul WD, Moore JJ, Lei MK. Mechanical and tribological properties of CrN/TiN multilayer coatings deposited by pulsed DC magnetron sputtering. Surf Coat Technol. 2015;276:152–9.
47. Hainsworth SV, Soh WC. The effect of the substrate on the mechanical properties of TiN coatings. Surf Coat Technol. 2003;163–164:515–20.

48. Miletić A, Terek P, Kovačević L, Vilotić M, Kakaš D, Škorić B, et al. Influence of substrate roughness on adhesion of TiN coatings. J Braz Soc Mech Sci Eng. 2014;36:293–9.
49. Shang W, Chen B, Shi X, Chen Y, Xiao X. Electrochemical corrosion behavior of composite MAO/sol–gel coatings on magnesium alloy AZ91D using combined micro-arc oxidation and sol–gel technique. J Alloy Compd. 2009;474:541–5.
50. Su J, Charmchi M, Sun H. A study of drop-microstructured surface interactions during dropwise condensation with quartz crystal microbalance. Sci Rep. 2016;6:1–11.
51. Mazumder A, Alangi N, Sethi S, Prabhu KN, Mukherjee J. Study on wettability of plasma spray coated oxide ceramic for hydrophobicity. Surf Interfaces. 2020;20:100591.
52. Kung KC, Lee TM, Lui TS. Bioactivity and corrosion properties of novel coatings containing strontium by micro-arc oxidation. J Alloys Compd. 2010;508:384–90.
53. Sowa M, Piotrowska M, Widziołek M, Dercz G, Tylko G, Gorewoda T, et al. Bioactivity of coatings formed on Ti-$_{13}$Nb-$_{13}$Zr alloy using plasma electrolytic oxidation. Mater Sci Eng C. 2015;49:159–73.
54. Dai N, Zhang LC, Zhang J, Chen Q, Wu M. Corrosion behavior of selective laser melted Ti-$_6$Al-$_4$V alloy in NaCl solution. Corros Sci. 2016;102:484–9.
55. Ramachandran R, Nosonovsky M. Coupling of surface energy with electric potential makes superhydrophobic surfaces corrosion-resistant. Phys Chem Chem Phys. 2015;17:24988–97.
56. Akaltun Y, Aslan M, Yetim T, Çayir T, Çelik A. The effect of wettability on corrosion resistance of oxide films produced by SILAR method on magnesium, aluminum and copper substrates. Surf Coat Technol. 2016;292:121–31.
57. Stalder AF, Melchior T, Müller M, Sage D, Blu T, Unser M. Low-bond axisymmetric drop shape analysis for surface tension and contact angle measurements of sessile drops. Colloids Surf A Physicochem Eng Aspects. 2010;364:72–81.
58. Han Y, Chen D, Sun J, Zhang Y, Xu K. UV-enhanced bioactivity and cell response of micro-arc oxidized titania coatings. Acta Biomater. 2008;4:1518–29.